

1 **REVISION II (FINAL)**

2
3 **Melting, Crystallization and the Glass transition:**

4 **Toward a Unified Description for Silicate Phase Transitions**

5 H. Wayne Nesbitt¹, G. Michael Bancroft², Grant, S. Henderson³, Pascal Richet⁴, Cedrick
6 O'Shaughnessy³

7
8
9
10 ¹Dept. of Earth Sciences, Univ. of Western Ontario, London On., N6A 5B7 Canada

11 ²Dept. of Chemistry, Univ. of Western Ontario, London On., N6A 5B7 Canada

12 ³Dept. of Earth Science, Univ. of Toronto, Toronto On., M5S 3B1 Canada

13 ⁴Institut de Physique du Globe de Paris, 1 Rue Jussieu, F-75252 Paris, France

14
15
16
17
18
19
20
21
22 **Corresponding Author:**

23 H. Wayne Nesbitt, Tel: (519) 661-2100 ext. 83194, e-mail: hwn@uwo.ca

25

26 **Keywords:** Premelting of minerals, Melting of minerals, melting mechanism, crystallization,
27 ²⁹Si NMR and Raman spectra of glasses and melts

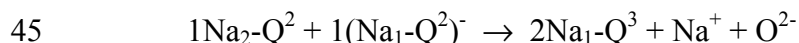
28 **ABSTRACT**

29 The melting mechanism of Na₂SiO₃, a crystal with pyroxene structure, includes three
30 distinct reactions. All are driven by heating with each reaction commencing at a different
31 temperature. The first two reactions proceed within the crystal at temperatures well below the
32 melting point and are expressed by distinctive crystallographic, calorimetric and Raman
33 spectroscopic changes in the crystal. With the reactions identified and explained for Na₂SiO₃(c)
34 and the melting mechanism elucidated, the Na₂SiO₃ system becomes the ‘Rosetta Stone’ by
35 which to decipher the melting mechanisms of all pyroxenes and other silicate minerals.

36 The first reaction produces itinerant Na⁺ within the crystal. Itinerancy results from
37 dissociation of some NBO-Na bonds due to heating, with dissociation commencing at ~770 K.
38 The reaction proceeds according to:

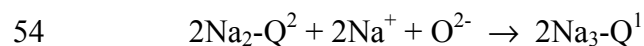


40 The Si-O⁻ moiety remains attached to its SiO₃ chain and it is charged because one of its NBO
41 atoms has no associated Na ion. The second reaction is characterized by the appearance of a Q³
42 band in Raman spectra of the crystal at temperatures >770 K. It is produced via a polymerization
43 reaction involving the Si-O⁻ species, a product of the first reaction, and a Q² species of an
44 adjacent SiO₃ chain according to:



46 Na atoms are included with each Q species to preserve mass balances and (Na₁-Q²)⁻ is equivalent
47 to the Si-O⁻ species. The produced Q³ species form cross-chain linkages which affect the
48 crystallographic properties of the crystal. They are responsible for the cessation of thermal

49 expansion of the Na₂SiO₃ unit cell in the ‘a’-‘b’ axial plane at T > 770 K, and the near-constancy
50 of ‘a’ and ‘b’ unit cell parameters between ~770 K and ~1300 K. The presence of Q³ species in
51 Raman spectra and the inhibited expansion in the ‘a’-‘b’ axial plane provide exceedingly strong
52 evidence for this reaction. The third reaction commences at ~1200 K where Q¹ Raman band first
53 appears. It can be produced *only* through depolymerization of Q² chains according to:



55 where Na⁺ and O²⁻ are itinerant species produced by the second reaction. With conversion of Q²
56 to Q¹ species, SiO₃ chains are ruptured, long range order is lost and melt is produced at 1362 K.

57 The last two reactions proceed by nucleophilic substitution where Si centers are attacked
58 to form 5-fold coordinated activated complexes. Si-O⁻ acts as nucleophile in the second reaction
59 (producing Q³ species), and O²⁻ acts as nucleophile in the third reaction (producing Q¹). Taken in
60 reverse, these mechanisms describe the formation of nuclei in crystallizing melts and in addition
61 provide insight into the elusive changes that occur at the glass transition. Elucidation of the
62 melting mechanism could thus provide a unified framework within which melting, crystallization
63 and the glass transition can be understood.

64 INTRODUCTION

65 From practical and theoretical perspectives, melting and crystallization are the most
66 important phase transitions. Silicates have a special importance in this respect as the concentric
67 structure of the Earth with a core, a mantle and a crust, the existence of SiO₂-rich, buoyant
68 continents and, thus, the subsequent emergence of life, are processes that were all ultimately
69 determined by melting and crystallization reactions. Today these reactions are also of utmost
70 importance as they are at the roots of the basic industries with annual production of nearly 3x10⁹
71 tons of cement, 4x10⁸ tons of iron and steel slags and about 10⁸ tons of glass. A comprehensive

72 theoretical framework within which to interpret melting, crystallization and vitrification
73 consequently would be of great benefit to Earth and materials scientists. We propose such a
74 framework by developing a melting mechanism applicable to numerous silicate minerals. It is
75 based in experimental results, thermodynamic constraints and on chemical kinetics principles.
76 The experimental results for Na_2SiO_3 are critically important to the development of the melting
77 mechanism. Our first objective consequently is to review the crystallographic, calorimetric and
78 Raman spectroscopic properties of Na_2SiO_3 between 298 K and its melting temperature (Richet
79 et al., 1996; McMillan, 1984; McDonald and Cruickshank, 1967). Once analysed and the
80 changes to the crystal elucidated, our second and most important objective, is to develop a
81 melting mechanism applicable to many silicate minerals through application of chemical kinetics
82 principles (Laidler, 1965) using the experimental results to constrain its development.

83 Physicists and chemists, for over a century, have studied the melting phenomenon for by
84 employing mostly physical principles, including vibrational instability, vanishing shear moduli
85 and defect production (Lindemann, 1910; Brillouin, 1938; Born, 1939; Lennard-Jones and
86 Devonshire, 1939; Frenkel, 1955; Eyring et al., 1958). None explains successfully the melting of
87 compositionally and structurally complex silicate minerals as emphasized by Wolf and Jeanloz,
88 (1984). There is, therefore, little or no understanding of how these silicates minerals melt. The
89 reason their melting is so poorly understood is that melting is too abrupt, and crystallization
90 begins with nuclei too small to be readily investigated by techniques available today. There are,
91 however, a few special cases whereby these reactions are more amenable to experimental
92 investigation. These manifest themselves in crystals with extensive premelting regions, which
93 may extend over tens to hundreds of degrees. (e.g., Thiéblot et al., 1999; Richet et al., 1996;
94 1994). Na_2SiO_3 is one such case. Crystalline sodium metasilicate (Na_2SiO_3) displays a large

95 premelting region of ~160 degrees and its structure is simple (Richet et al., 1996) making
96 detailed structural, calorimetric and spectroscopic studies possible over a wide range of
97 temperature (Figs. 1a, 1b). From such results we identify three reactions which are *necessary*
98 *precursors* to the melting of Na₂SiO₃. Perhaps most importantly, each reaction is initiated at a
99 different temperature permitting detailed investigation of each without appreciable overlap or
100 interference from the other reactions. Taken in reverse, the same reactions account for the
101 formation of nuclei in melts and subsequent crystallization. The steps are also applicable to
102 changes that occur at the glass transition, including structural relaxation and viscous flow, thus
103 providing a unified description and theory of these phenomena.

104 **STRUCTURE OF Na₂SiO₃**

105 The Si-O structural arrangements of crystalline Na₂SiO₃ are identical to those of the
106 pyroxene group of minerals. It consists of chains of Si tetrahedra (McDonald and Cruickshank
107 1967; Ching et al., 1983) where two apical oxygen atoms bridge two Si atoms (bridging oxygens
108 or BO) to produce Si-O-Si moieties and to form SiO₃ chains parallel to the c axis as shown
109 schematically in Figure 2a. The two other oxygen atoms of each tetrahedron are bonded to a Si
110 and a Na atom to produce the Si-O-Na moiety whose oxygen is referred to as non-bridging
111 (NBO). Na atoms are encased in oxygen bipyramids and are located between the chains binding
112 them together. The crystal's cell parameters increase systematically with temperature to ~770 K
113 (Fig. 1a). The 'c' cell parameter continues to increase without inflection to at least 1300 K
114 (Richet et al., 1994; 1996). The 'a' and 'b' cell parameters, by contrast, remain effectively
115 constant between about ~770 K and ~1300 K (Fig. 1a). There is also a change in space group at
116 ~850 K from *Cmc* 2₁ to a lower symmetry, probably to *Pmc* 2₁ (Richet et al., 1996). With
117 transition to lower symmetry, there is loss of a Na position in the 'a'-'b' axial plane.

118 **Na₂SiO₃ HEAT CAPACITY AND ITINERANT Na⁺**

119 The mean heat capacities (C_m) for four crystalline phases are plotted against temperature
120 in Figure 1b, where C_m is defined as $(H_T - H_{273}) / (T - 273)$ with H being enthalpy (Richet and
121 Fiquet, 1991). The heat capacities of all crystals initially change as expected with respect to
122 temperature, due primarily to acoustic vibrational contributions but on approach to the melting
123 point, each displays a dramatic increase in C_m . The inflection in C_m for Na₂SiO₃(c) occurs at
124 ~1200 K and the region between the inflection and the melting point (1362 K) is defined as the
125 *premelting region*. Many other minerals display premelting regions (Bouhifd et al., 2002;
126 Thiéblot et al., 1999; George et al., 1998; Richet et al., 1998; 1996; 1994; 1993). The ²³Na NMR
127 study of George et al. (1998) demonstrate cation itinerancy within the premelting region of
128 Na₂SiO₃. They note that “Na⁺ site hopping appears to involve a more liquid-like behavior,
129 implying exchange occurred among many sites (i.e., itinerancy) with different orientations, and
130 in a disordered fashion”. Na⁺ itinerancy in crystals apparently is analogous to Na⁺ mobility in
131 glass as simulated by Cormack et al. (2002) where they monitored alkali ion ‘jumps’ to adjacent
132 empty sites of variable potential energy. The data of George et al. (1998) are conclusive but a
133 question arises concerning the temperature at which itinerancy is initiated. The structural data,
134 particularly thermal expansion characteristics (Fig. 1a), indicates a significant change in crystal
135 properties at ~770 K and this may reflect the onset of itinerancy. The suggestion is reinforced by
136 loss of a Na position in the ‘a’-‘b’ axial plane at ~850 K.

137 The temperature at which Na⁺ itinerancy is initiated must relate to the weakness of Na-O
138 bonds. Crystalline Li₂SiO₃ and Na₂SiO₃, for example, share the same structure but upon heating
139 there is no indication of Li⁺ itinerancy, and no change in space group in the temperature range
140 298 K to the melting point. The Na-O bond dissociation energy is 257 kJ/mol whereas that of Li-

141 O is 341 kJ/mol (Speight, 2005). With heating and vibrational excitation, Na-O bonds are
142 therefore expected to dissociate at lower temperatures than Li-O bonds (and to greater extent at
143 the same temperature). Dissociation may be represented by the reaction:



145 To maintain mass balances, Na atoms attached to each Q species should be included so that:



147 where a Si-O-Na moiety incorporated into the $\text{Na}_2\text{-Q}^2$ species dissociates yielding a charged
148 $(\text{Na}_1\text{-Q}^2)^-$ species and Na^+ . In summary, it is established that Na-O dissociation occurs (George et
149 al., 1998; Richet et al., 1996) and structural changes to the crystal (e.g., Fig. 1a) suggest that it
150 commences at ~770 K. Increased temperature drives Reaction (1) to the right thus increasing
151 itinerancy and promoting structural change such as that evident at ~850 K where there is loss of
152 an Na position in the ‘a’-‘b’ axial plane of the crystal (Richet et al., 1996).

153 Dissociation of each Na-O bond necessarily produces a Si-O^- moiety which, while still
154 attached to a chain, should undergo librations unavailable to the Si-O-Na moiety due to the loss
155 of a bonding partner (Na) and to the presence of an ‘exposed’ negative charge on the NBO.
156 Additional librations in the premelting region were confirmed by ^{29}Si NMR results of George et
157 al. (1998) where partial averaging of low temperature biaxial chemical shifts occur, “suggesting
158 some kind of extensive, librational motion of SiO_4 tetrahedra”. In addition, progressive heating
159 causes many weak, low to intermediate frequency Raman Na-O bands to broaden or merge into
160 the spectral background (Richet et al., 1996). The Si-O^- species is negatively charged and may
161 act as a nucleophile in chemical reactions, as emphasized subsequently.

162 **RAMAN SPECTRA OF Na_2SiO_3**

163 Previously published ^{29}Si NMR and Raman spectra of Na_2SiO_3 crystal and glass (Figs.

164 3a, 3b, 3c) contain valuable information concerning reactions that occur in the crystal during
165 heating to the melting point. This was not realized previously because the spectral similarities
166 between crystal and glass had not been recognized (spectra from Nesbitt et al., 2011; Richet et
167 al., 1996; Frantz and Mysen, 1995). We emphasize these similarities and begin by addressing the
168 ^{29}Si MAS NMR and Raman spectra of Na_2SiO_3 glass (Figs. 3a, 3b) followed by interpretation of
169 the Raman spectrum of crystalline Na_2SiO_3 (Fig. 3c).

170 **Na_2SiO_3 Glass Spectra.**

171 **Assignment of Bands.** The ^{29}Si MAS NMR spectrum of the glass (Fig. 3a) was fit by Nesbitt et
172 al. (2011) employing three symmetric 100% Gaussian peaks. Once the spectrum was fit, the
173 peaks were assigned to Q^1 , Q^2 and Q^3 species based on peak position. Maekawa et al. (1991)
174 arrived at precisely the same assignments. The two studies demonstrate that there are three major
175 contributions to the glass spectrum, the Q^1 , Q^2 and Q^3 species signals and also demonstrate that
176 no other Q species makes major contribution to the glass spectrum.

177 Comparison of Figures 3a and 3b reveal similarities between the ^{29}Si MAS NMR and
178 Raman spectra of Na_2SiO_3 glass (Nesbitt et al., 2011; Frantz and Mysen, 1995; Maekawa et al.,
179 1991). Each displays a strong central peak with a shoulder on the high frequency side of the
180 central peak, and a weak peak on the low frequency side. The similarity is expected because the
181 signals for both spectra arise from the same sources, the Q species; that is, the three Q species
182 observed in the ^{29}Si NMR spectrum of Figure 3a must also contribute to the Raman spectrum of
183 Figure 3b. It is therefore reassuring that the two figures have similar characteristics. The results
184 of Brawer and White (1975) provide the information needed to identify the approximate location
185 of the three Q species contributions in the Raman spectrum of the glass (Fig. 3b). These authors
186 collected Raman spectra of crystalline and vitreous Na_2SiO_3 at ambient temperature. The crystal

187 contains only the Q^2 species whose peak is centered at 975 cm^{-1} . Their glass spectrum displays
188 its most intense peak at 985 cm^{-1} . At this composition the Q^2 band is expected to be the most
189 intense. On this basis, and on the similarity of peak positions in crystal and glass, we propose
190 that the Q^2 species is the major contributor to the 985 cm^{-1} peak of their Na_2SiO_3 glass (i.e., Q^2
191 species is assigned to the 985 cm^{-1} band).

192 Turning to Figure 3b and focussing on the experimental results (dots), we find that the
193 most intense experimental signal is centred at $\sim 966\text{ cm}^{-1}$. By comparison with the glass spectrum
194 of Brawer and White (1975), and based on peak position and intensity, we assign the Q^2 signal to
195 the 966 cm^{-1} band. With its position established, the other contributions to Figure 3b can be
196 assigned. Brawer and White (1975) observe a peak at 855 cm^{-1} in their glass spectrum, which is
197 located at $\sim 130\text{ cm}^{-1}$ lower frequency than the Q^2 band. Figure 3b has a peak at $\sim 842\text{ cm}^{-1}$. It is
198 $\sim 124\text{ cm}^{-1}$ lower in frequency than the Q^2 band. McMillan (1984) locates the Q^1 band at ~ 50 - 100
199 cm^{-1} lower frequency than the Q^2 band. Thus the 842 cm^{-1} peak of Figure 3b is assigned to the Q^1
200 species. McMillan (1984) also notes that the Q^3 band is located at ~ 50 - 100 cm^{-1} greater
201 frequency than the Q^2 band, thus the Q^3 band of Figure 3b should be present at ~ 1015 - 1065 cm^{-1} ,
202 and within the pronounced shoulder on the high frequency side of the Q^2 band. A better estimate
203 of the location of the Q^3 peak can be obtained by fitting parts of the spectrum.

204 **Partial Fit to the Spectrum.** The Raman spectrum (Fig. 3b) was fit using 100% Gaussian
205 lineshapes. The shape may not be optimum but it is sufficient for our purpose. A Q^1 peak was
206 introduced and centered at $\sim 842\text{ cm}^{-1}$. Its FWHM was adjusted manually to fit as closely as
207 possible the experimental peak. The fitted peak has a linewidth of $\sim 36\text{ cm}^{-1}$. We then added a Q^2
208 peak, the position and Full Width at Half Maximum (FWHM) of which were constrained to fit
209 the high frequency side of the most intense peak. The resulting peak position is $\sim 966\text{ cm}^{-1}$ and its

210 FWHM is $\sim 41 \text{ cm}^{-1}$. The positions of the Q^1 and Q^2 peaks are consistent with those quoted by
211 McMillan (1984). We introduced a third peak to represent the Q^3 (highest frequency) band. Its
212 intensity, FWHM and location were constrained as follows. The Q^3 intensity of the ^{29}Si MAS
213 NMR spectrum (Fig. 3a) is 5.2 times more intense than that of the Q^1 peak. Assuming the Raman
214 scattering factors for the Q^1 and Q^3 peaks are similar (i.e., 1:1 ratio) we constrained the Raman
215 Q^3 band of Figure 3b to have an intensity 5.2 times greater than that of the Q^1 band of the
216 Raman spectrum. There is no detectable Q^4 signal in the NMR spectrum of Na_2SiO_3 glass (Fig.
217 3a) so that the Q^3 species is considered the highest frequency contribution to Figure 3b. The
218 linewidth of the Q^3 peak was therefore adjusted to fit the highest-frequency portion of the
219 spectrum while maintaining the appropriate peak intensity, thus yielding the peak represented by
220 the solid curve of Figure 3b. It is centered at $\sim 1030 \text{ cm}^{-1}$ with FWHM of 94 cm^{-1} and is
221 consistent with the Q^3 peak position quoted by McMillan (1984).

222 The greatest uncertainty related to fitting the Q^3 peak is the assumption that scattering
223 factors are the same for the Q^1 and Q^3 bands. To determine the sensitivity of this assumption, we
224 alternatively employed the scattering factors of Koroleva et al. (2013), which are 1.53 for Q^1 and
225 1.0 for Q^3 . From the Q^1 and Q^3 areas of Figure 3a and these scattering factors, the Q^3 peak area
226 should be 3.5 greater than the Q^1 peak area in Figure 3b. With this constraint, the resulting best
227 fit for the Q^3 band is shown as the dashed curve centered at $\sim 1048 \text{ cm}^{-1}$ (FWHM $\sim 81 \text{ cm}^{-1}$). The
228 Q^3 peak position of the glass therefore is reasonably well established to reside between ~ 1030
229 cm^{-1} and $\sim 1050 \text{ cm}^{-1}$ regardless of the scattering factors used. The position is consistent with the
230 Q^3 position noted by McMillan (1984). The approximate locations of the three Q species have
231 been ascertained. Additional contributions to the Raman spectrum are required to complete the
232 fit, which will be provided in a future publication. (e.g., Fig. 4 of Koroleva et al., 2013; Fig. 12

233 of Richet et al., 1996). Although our fit is not complete, three important conclusions nevertheless
234 can be drawn from the partial fit: (1) the peak assignments are consistent with the ^{29}Si NMR
235 spectra of Maekawa et al. (1991) and Nesbitt et al., (2011) as apparent in Figure 3a; (2) the
236 Raman Q species peak positions are reasonably well established and agree with those previously
237 reported by McMillan (1984); (3) the intensity of the Q^3 band is greater than that of the Q^1 band.

238 **Crystalline Na_2SiO_3 Spectrum.**

239 **Introduction.** Raman spectra for crystalline Na_2SiO_3 (e.g., Fig. 3c) were collected at
240 temperatures ranging from 298 K to the melting point (1362 K) by Richet et al. (1996). The 298
241 K spectrum displays an exceedingly intense band representing the Si-O symmetric stretch of the
242 Q^2 species. The band is located at $\sim 965\text{ cm}^{-1}$, has a FWHM of 6 cm^{-1} and its shape is strongly
243 Lorentzian (Richet et al., 1996). The spectrum in Figure 3c is that of crystalline Na_2SiO_3
244 collected at 1348 K (just below its melting point). With heating a new band appears at $\sim 770\text{ K}$
245 which is centered at $\sim 1030\text{ cm}^{-1}$ (Richet et al., 1996). The band becomes more intense with
246 temperature and is most intense in the premelting region. At $\sim 1200\text{ K}$, another band develops at
247 $\sim 900\text{ cm}^{-1}$. Its intensity increases with temperature but it never approaches the intensity of the
248 band at $\sim 1030\text{ cm}^{-1}$.

249 **Fitting the Spectrum.** Following Richet et al. (1996), three entirely *unconstrained*, 100%
250 Lorentzian peaks were introduced to fit the spectrum. The resulting least squares fit is shown in
251 Figure 3c. The most intense fitted peak, centered at 959 cm^{-1} , represents the Q^2 signal (Richet et
252 al., 1996). Its FWHM is $\sim 37\text{ cm}^{-1}$ and it represents $\sim 68\%$ of the spectral intensity. McMillan
253 (1984) states that the Q^3 signal is situated at 50-100 cm^{-1} greater frequency than the Q^2 signal in
254 the glass, and if present in Figure 3c, it should be located between about $\sim 1010\text{ cm}^{-1}$ and ~ 1060
255 cm^{-1} . The *unconstrained*, fitted peak centred at $\sim 1031\text{ cm}^{-1}$ is entirely consistent with it being a

256 Q³ signal and we interpret it as such. The location of the Q³ peak for the glass (Fig. 3b) and the
257 crystal (Fig. 3c) is similar, reinforcing the Q³ species assignment. The Q³ peak of the crystal has
258 a FWHM of ~86 cm⁻¹ and its intensity constitutes ~22% of the total signal.

259 The third *unconstrained* peak fitted to the spectrum is centered at ~905 cm⁻¹. It has a
260 FWHM of 65.4 cm⁻¹ and constitutes ~10% of the total signal. McMillan (1984) states that the Q¹
261 signal is located at 50 to 100 cm⁻¹ lower frequency than the Q² band, thus the peak centred at
262 ~905 cm⁻¹ is consistent with it being a Q¹ peak and we interpret it as such. The Q³ peak intensity
263 is appreciably greater than the Q¹ intensity and it remains to explain how Q³ and Q¹ species are
264 produced in the crystalline chain silicate Na₂SiO₃ near its melting point. With the three Q species
265 contributing to the crystal reasonably well established, insight into the reactions occurring within
266 the crystal in response to thermal input can be evaluated.

267 THE MECHANISM – STEP I: Q³ AND O²⁻ PRODUCTION

268 The implications of the similarities between the Raman spectra of crystalline and vitreous
269 Na₂SiO₃ (Figs. 3b and 3c) are now addressed in more detail than originally provided (Richet et
270 al., 1996). Between ambient temperature and ~770K only a strong Q² peak is observed in the
271 Raman spectrum of Na₂SiO₃ (Richet et al., 1996, their Fig. 6). Above ~770 K a Q³ band appears
272 and its intensity increases dramatically within the premelting region. There is *no* Q¹ band present
273 in spectra collected below ~1200 K and in the absence of a Q¹ band, the *only means to produce*
274 *Q³ species* in the crystal, without producing an equal amount of Q¹ species, is via a
275 polymerization reaction involving Q² species. If (Na₁-Q²)⁻ (or alternatively Si-O⁻) produced by
276 reaction (1) were to react with another Q² species (i.e., Na₂-Q²) then:



278 The (Na₁-Q²)⁻ moiety is a nucleophilic agent and is likely to react with Si centers as explained

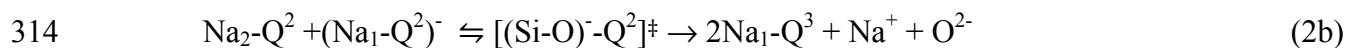
279 subsequently in the ‘Reaction Mechanism’ section. The reaction produces an itinerant Na^+ and
280 itinerant O^{2-} . The reaction obviously requires structural changes to the crystal to accommodate
281 the Q^3 species.

282 **Structural Effects.** As observed in double chain silicates (e.g., amphiboles, Deer et al.,
283 2013), the Q^3 species in Na_2SiO_3 likely form cross-chain linkages in the ‘a’-‘b’ axial plane as
284 shown schematically in Figure 2b. These cross-chain linkages should inhibit or prevent
285 expansion of the Na bipyramids along their polar axes in the ‘a’-‘b’ axial plane but they should
286 not inhibit expansion along the ‘c’ polar axis. The formation of Q^3 cross-chain linkages
287 consequently provides the explanation for the unusual changes observed in the unit cell thermal
288 expansion coefficients of Figure 1a; that is, all three a, b and c cell parameters increase as
289 expected up to ~ 770 K. Once Q^3 species begin to form there is minimal increase in the ‘a’ and
290 ‘b’ cell parameters but the ‘c’ cell parameter continues to increase without inflection at ~ 770 K.

291 The Si-O-Si and O-Si-O bond angles may be distorted due to Q^3 cross-chain linkages but
292 they need not disrupt the structure of the crystal. Indeed, the pyroxene structure of Na_2SiO_3 is
293 maintained to its melting temperature (George et al., 1998; Richet et al., 1996). If formed
294 randomly along the chains, the cross linkages would not be detectable by X-ray diffraction
295 methods. The effects of Reactions (1) and (2) on structure thus are elucidated and the
296 relationships between Q^3 production and properties of the unit cell parameters are established.

297 **Reaction Mechanism.** The Si-O bonds of the Si-O-Si and Si-O-Na moieties have
298 substantially different bonding character as evident from O 1s X-Ray Photoelectron spectroscopy
299 (XPS) results for Na_2SiO_3 glass where O 1s photoelectrons derived from BO and NBO differ by
300 ~ 1.8 eV in binding energy (Nesbitt et al., 2011; 2015a). The valence electron density over NBO
301 is consequently greater than over BO so that NBO has the greater ionic character. Oxygen is

302 more electronegative than Na^+ so that upon Na-O bond dissociation, NBO retains its negative
303 charge. With retention of the charge, the $(\text{Na}_1\text{-Q}^2)^-$ or Si-O^- moiety produced by Reaction (1a)
304 becomes a strong *nucleophile*. Si tetrahedra are Si sp^3 hybridized and nucleophilic substitution
305 commonly occurs on sp^3 hybridized species (Huheey et al., 1993; Chuit et al., 1993; Corriu,
306 1990). At high temperature, the nucleophile, Si-O^- , likely attacks Si of Q^2 tetrahedra in adjacent
307 SiO_3 chains to form a 5-coordinate Si-O moiety (Chuit et al., 1993; Corriu, 1990). In support of
308 the suggestion, Si-O pentahedra are observed in some zeolites at ambient temperature (Fyfe et
309 al., 2002), in K and Na silicate glasses at ambient temperature and pressure (Stebbins, 1991) and
310 in Na-silicate melts subjected to high pressure (Wolf et al., 1990). We propose that the Q^3
311 species observed in the Raman spectra of Na_2SiO_3 are produced by a nucleophilic substitution
312 reaction. It occurs through attack of a charged Q^2 species, $(\text{Na}_1\text{-Q}^2)^-$, produced by Reaction (1)
313 on a Si center of a Q^2 species according to:



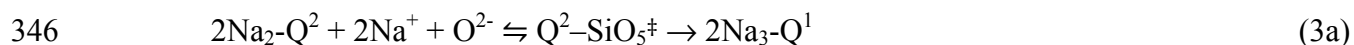
315 where $[(\text{Si-O})^-\text{-Q}^2]^\ddagger$ is the transition state (activated) complex illustrated schematically in Fig. 2c.
316 Reaction (2a) is the stoichiometric equivalent of Reaction (2b). The activated complex may
317 decompose to its reactants (indicated by \rightleftharpoons) but occasionally it may proceed to the final products,
318 namely, Na^+ , O^{2-} and Q^3 (Fig. 2b). The leaving species ($\text{Na}^+ + \text{O}^{2-}$), along with the itinerant Na^+
319 produced by Reaction (1), yield two itinerant Na^+ and an itinerant O^{2-} as products. Si-O^- is
320 generated by Na-O dissociation and its abundance increases with temperature, driving Reaction
321 (2b) to the right. Steric hindrance may inhibit nucleophilic attack but the reaction is promoted at
322 high temperature by the short lifetime of Si-O bonds (Farnan and Stebbins, 1990).

323 The hypothesis is corroborated by molecular-dynamics (MD) simulations of Na_2SiO_3
324 melt at 2000 K. According to Berezhnoi and Boiko (2005), when two Si tetrahedra approach, the

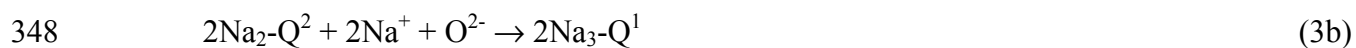
325 non-bridging oxygen (Si-O⁻) of one tetrahedron attacks the Si center of another tetrahedron to
326 form a 5-fold coordinated Si pentahedron (the activated complex of Reaction 2b and Fig. 2c).
327 Immediately, one of the other Si-O bonds is severed to reform a tetrahedrally coordinated Si
328 center. The details of the mechanism by which Reaction (2b) proceeds is uncertain but likely
329 follows a S_N2 mechanism (Laidler, 1965), although this remains to be proved. The mechanism
330 involves an elementary (single step), bi-molecular reaction the details of which are lucidly
331 presented by Laidler (1965, p. 144-163).

332 **THE MECHANISM – STEP II: Q¹ PRODUCTION AND MELTING**

333 Melting of Na₂SiO₃ requires rupture of the Si-O-Si bonds of its SiO₃ chains. With a bond
334 dissociation energy of 798 kJ/mol (Speight, 2005) Si-O bonds are unlikely to be ruptured unless
335 they undergo nucleophilic attack (Corriu, 1990). Above ~770 K, Reaction (2) is active and
336 itinerant O²⁻ is present in the crystal. Free oxygen is a stronger nucleophile than Si-O⁻ and is less
337 affected by steric hindrance due to its smaller size. Furthermore, the O²⁻ produced by Reaction
338 (2) finds no available structural site in crystalline Na₂SiO₃; it is itinerant and available for
339 nucleophilic attack on tetrahedrally coordinated, sp³ hybridized Si centres (Corriu, 1990; Chuit et
340 al., 1993). Nucleophilic attack forms a 5-coordinate transition state (activated) complex (SiO₅[‡])
341 as shown in Figures 4a and 4c. The activated complex, SiO₅[‡], once formed may occasionally
342 decompose to form Q¹ species via Reaction (3) through rupture of a Si-BO bond of the activated
343 complex (SiO₅[‡]); production of Q¹ species, *necessarily* fragments the SiO₃ chain (Fig. 4b). With
344 sufficient O²⁻, formation of Q¹ continues and the SiO₃ chains eventually lose their integrity, long-
345 range structure is lost, and melt is produced (illustrated in Figure 4). The reaction is:



347 and omitting the activated complex:



349 Na atoms are associated with the Q species to maintain mass balances. The Raman spectrum of
350 Figure 3c was collected in the premelting region of Na_2SiO_3 where **the crystal** still retained its
351 structural integrity, yet a small Q^1 signal is apparent. Within the premelting region, the intensity
352 of this band increases with temperature (Richet et al., 1996, their Fig. 6). The weak Q^1 signal
353 suggests that SiO_3 chains have been ruptured in a few places prior to melting, but not in
354 sufficient quantity to destroy long-range order, possibly because the Q^3 cross linkages already
355 formed help to stabilize the few segmented chains. The Q^1 band (Fig. 3c) is strong evidence that
356 Reaction (3) occurs while Na_2SiO_3 is crystalline. There can be little doubt that this reaction also
357 proceeds at its melting point. With production of sufficient Q^1 species, the long range order of
358 the crystal must be lost and a melt produced. We conclude that destruction of the SiO_3 chains and
359 melting of crystalline Na_2SiO_3 occur through nucleophilic attack on Si centers by the very strong
360 nucleophile, O^{2-} . Involvement of O^{2-} and $(\text{Na}_1\text{-Q}^2)^-$ in Reaction (2) likely occurs through a $\text{S}_{\text{N}}2$
361 mechanism (Laidler, 1965). Molecular dynamics simulations on Na_2SiO_5 melt (Berezhnoi and
362 Boiko, 2005) support strongly such a mechanism as they reveal the presence of O^{2-} , which
363 attacks Si centers of tetrahedral chains as proposed for the melting by Reaction (3).

364 Effects prior to melting are exceedingly important in that the strong nucleophile, O^{2-} , is
365 produced beginning at ~ 770 K (Rxn 2) at a rate that depends ultimately on the strength of the
366 Na-O bond and temperature. The cation becomes itinerant, cross-linking of chains becomes
367 feasible with production of Si-NBO^- and, thanks to such cross-linking, O^{2-} is produced via
368 Reaction (2). As temperature increases, the itinerant O^{2-} builds until a sufficient concentration is
369 achieved to sustain the production of SiO_5^\ddagger and, ultimately, the production of Q^1 and rupture of
370 the SiO_3 chains. At melting, a steady state is achieved because production of O^{2-} (via Rxn. 2) is

371 balanced by its consumption (via Rxn 3). The stoichiometric reaction *at the melting point* then is:



373 where the O^{2-} concentration is constant as melting proceeds. Free oxygen (O^{2-}) is a critical
374 constituent in the proposed mechanism. This exceptionally strong nucleophile is the primary
375 agent causing depolymerization of the SiO_3 chains and ultimately melting. It is generated in the
376 crystal through formation of cross-chain linkages (Rxn 2) as revealed by the presence of Q^3
377 species in high temperature Raman spectra of $Na_2SiO_3(c)$ (Richet et al., 1996). Involvement of
378 free oxygen in melting is proved by its presence at the mol% level in binary silicate melts and
379 their quenched glasses (Nesbitt et al., 2015a; 2015b; 2015c; 2011; Retsinas et al., 2014; Al-Hasni
380 and Mountjoy, 2014; Sawyer et al., 2012; 2015; Nasikas et al., 2012; 2011; Davis et al., 2011;
381 Sen et al., 2009; Kalampounias et al., 2009; Sen and Tangeman, 2008). The amount of O^{2-}
382 present in the melt will dependent on the equilibrium constants of Reactions (2) and (3).

383 **MELTING OF OTHER SILICATES**

384 Lithium metasilicate is isostructural with Na_2SiO_3 but bond distances are shorter and Li is
385 tetrahedrally coordinated with oxygen (Richet et al., 1996). Extending the arguments derived
386 from the $Na_2SiO_3(c)$ Raman spectrum (Fig. 3c), we note that the $Li_2SiO_3(c)$ includes a weak Q^3
387 band in its Raman spectrum collected just below its melting point indicating the formation of
388 cross-chain linkages and production of itinerant Li^+ and O^{2-} (Richet et al., 1996, their Fig. 12).
389 Because of the greater dissociation energy of Li-O (341 kJ/mol) compared to that of Na-O (257
390 kJ/mol), lithium mobility is lower in the Li_2SiO_3 crystal, thus no phase transition takes place, and
391 no nucleophilic agent (e.g., $Si-O^-$ or O^{2-}) is produced until the premelting region is encountered
392 (which extends ~ 10 K below the melting point). All of Reactions (1), (2) and (3) are thus
393 constrained to a very small thermal window of ~ 10 K. Within this window, the reactions are

394 initiated and melting occurs over such a small temperature range that they cannot be followed
395 experimentally. Thus melting of Li_2SiO_3 is sharper than that of Na_2SiO_3 (Téqui et al., 1992). In
396 summary, the greater dissociation energy of Li-O (341 kJ/mol) relative to Na-O (257 kJ/mol)
397 confines all reactions, and the associated melting mechanisms, to a span of a few degrees. The
398 melting of Li_2SiO_3 thus is a counterpoint to Na_2SiO_3 whose reactions occur over an extended
399 temperature range.

400 Pseudowollastonite (CaSiO_3) contains 3-membered rings of Q^2 species (Seryotkin, 2012)
401 and it displays a premelting region extending from ~ 1570 K to its melting point of 1820 K (Fig.
402 1a; Richet et al., 1998). Ca-O bond lengths vary from ~ 2.28 to ~ 2.68 Å (Yang and Prewitt,
403 1999). With heating, Ca associated with the longest bonds may become itinerant allowing an
404 analog of Reaction (1) to occur. As evidence, Bouhifd et al. (2002) observed an increase in Ca
405 self-diffusion within the crystal beginning at ~ 1570 K which implies initiation of Ca-O bond
406 dissociation and Ca itinerancy. Raman spectra of CaSiO_3 (Richet et al., 1998, their Fig. 10)
407 collected within its premelting region indicates development a Q^3 band as observed for Na_2SiO_3
408 (Fig. 3c). These observations are taken as evidence that a reaction analogous to Reaction (2)
409 occurs in the premelting region whereby Q^3 , Ca^{2+} and O^{2-} are produced with the Q^3 species
410 forming linkages connecting adjacent rings. The cross linkages seem to affect most the 'b' polar
411 dimension because the 'b' cell parameter ceases to expand (and may contract) within the
412 premelting region (Richet et al., 1998, their Fig. 2). With production of O^{2-} , a reaction analogous
413 to Reaction (3) likely occurs, producing Q^1 species, dismemberment of the rings, and melt.

414 Diopside ($\text{CaMgSi}_2\text{O}_6$) melts much like Na_2SiO_3 and CaSiO_3 . Dimanov and Ingrin (1995)
415 demonstrated that upon heating, a substantial change in Ca self-diffusion occurred within
416 diopside beginning at ~ 1515 K (melts at 1670 K). The enhanced mobility of Ca may represent

417 the onset of Ca-O bond dissociation and production of itinerant Ca. Diopside premelting begins
418 at ~1530 K (Fig. 1b) and a weak signal develops on the high frequency side of the Q² peak as the
419 melting temperature (1670 K) is approached (Richet et al., 1998, their Fig. 6). Its location is
420 consistent with the Q³ band frequency in Raman spectra of Na₂SiO₃ (e.g., Fig. 3c) and its
421 presence provides evidence that a reaction equivalent to Reaction (2) occurs in the premelting
422 region of diopside. The reaction produces O²⁻ and with its presence, a reaction equivalent to
423 Reaction (3) may cause rupture of Q² chains and melting. Melting of diopside is, however,
424 slightly incongruent and is more complex than here portrayed.

425 Protoenstatite (MgSiO₃) melts congruently but metastably at ~1816 K and demonstrates
426 a premelting region beginning at ~ 1700 K (Thiéblot et al., 1999). Thiéblot et al. (1999) note that
427 onset of premelting correlates with enhanced Mg mobility (itinerancy) implying that some Mg-O
428 bond dissociation occurs with necessary production of SiO₃⁻, which in turn allows for production
429 of Q³ cross linkages and O²⁻ production via Reaction (2). Protoenstatite may undergo melting by
430 the same mechanism as the other pyroxenes.

431 A different situation obtains for orthosilicates such as olivine, which consist of Q⁰
432 species. A reaction analogous to Reaction (3) cannot occur for lack of O²⁻. Similarly, these
433 mechanisms are inapplicable to SiO₂ polymorphs and tectosilicates in which alkalis have a very
434 low mobility as a result of their charge-compensating role for aluminum in tetrahedral
435 coordination (Richet and Mysen, 1999). These minerals do not undergo premelting, and melting
436 and precipitation are sluggish (Bourova et al., 2006; Schairer and Bowen, 1956). A surface
437 melting mechanism rather than a bulk melting mechanism has been described for quartz and
438 cristobalite (Wagstaff, 1969; Ainslie et al., 1961). These crystals lack a simple mechanism to
439 produce free oxygen thus they provide circumstantial evidence for the critical role of the anion

440 (O^{2-}) in melting and crystallization of the chain silicates.

441 **DISCUSSION WITH IMPLICATIONS**

442 At the congruent melting point the fusion and crystallization reactions are by definition
443 reversible. This macroscopic reversibility implies that the mechanisms involved in the solid-
444 liquid transformation are also reversible, in agreement with the fact that the relevant constituents
445 such as Q species, itinerant cations and O^{2-} species are present in both Na_2SiO_3 crystals and
446 melts (Fig. 3). The first consequence is that determination of long-range order within growing
447 nuclei would bring little information on the actual crystallization mechanisms at play, which
448 involve instead complex, short-range order rearrangements. The second is that, even with current
449 technology, it would be a formidable task to investigate the relevant reactions and the ensuing
450 variations of short-range order within nanoscale nuclei that represent a negligible volume
451 fraction of the system at the onset of crystallization. To obviate this problem, monitoring the
452 abundances of critical species such as the Q species and O^{2-} during slow cooling of a melt might
453 be a more fruitful approach. In the favorable cases where premelting is significant, however, the
454 most straightforward way to study crystallization is to investigate instead fusion through
455 premelting and melting reactions which, their sense notwithstanding, are the same whether the
456 material is heated or cooled. Finally, the complete failure of nucleation theories to predict
457 nucleation rates, which can be 10^{20} - 10^{50} times greater than observed, has been repeatedly stated
458 (Fokin et al., 2006). In this respect a major source of discrepancy could be the neglect of such
459 reactions as (1-4) rather than the roughness of the liquid-nuclei interface, variations of surface
460 energy with temperature and the size of nuclei, or initial nucleation of metastable crystals.

461 These suggestions have bearing on the other major solidification process, namely,
462 vitrification. At the glass transition, variations in second-order thermodynamic properties occur

463 when the configuration of the silicate framework becomes frozen in (Richet and Neuville, 1992).
464 By contrast the mobility of network-modifier cations, hence electrical conduction, is much less
465 affected at the transition (Bouhifd et al., 2002; Gruener et al., 2001). The experimental results for
466 the alkali metasilicate crystals point to this conclusion in that only the rates of Reactions (2) and
467 (3) involving Q species increase markedly at the onset of premelting while network-modifier
468 cations remain highly mobile across the transition.

469 That the analogy is even deeper is indicated by the role played in these reactions by five-
470 coordinate Si atoms. Activated complexes are essential to the proposed melting and
471 crystallization mechanisms and they are a key factor in the configurational rearrangements
472 involved in viscous flow (Fokin et al., 2006). Reactions of the kind described here likely
473 contribute to the configurational changes characteristic of the liquid phase, and particularly to
474 their calorimetric effects. A connection between melting and viscosity mechanisms has been
475 drawn recently (Buchenau et al., 2014) from a reformulation of Lindemann criterion (in terms of
476 shear moduli) without, however, making room for distinct reaction steps such as proposed here.
477 Insights may also be gained from theoretical and molecular dynamics simulations if they were to
478 incorporate the properties of the three types of reaction and the bonds in chain silicates (e.g., Na-
479 O, Si-NBO, Si-O in Na_2SiO_3). A consistent description of melting, crystallization and glass
480 transition seems possible, combining kinetic, thermodynamic, transport and structural properties.

481 To understand better the melting, crystallization and vitrification of silicates, chemical
482 species and their abundances should be monitored as a function of temperature above *and* below
483 melting points. Melting, crystallization and vitrification of compositionally complex silicates are
484 better addressed via chemical mechanisms and orbital hybridization (Richet and Ottonello, 2014;
485 Koroleva et al., 2013) than via mechanical mechanisms (e.g., vibrational instability).

486

ACKNOWLEDGMENTS

487 Thanks are due to B.O. Mysen who kindly retrieved Raman data of previous
488 investigations and to R. Conradt, R. Kerner, G. Ottonello, and A. Takada for helpful comments.
489 We also thank two reviewers and the managing editor for their comments, which resulted in
490 substantial improvement to the presentation. Logistical support for this publication came from
491 the Univ. of Western Ontario (H.W.N., G.M.B.) and Univ. of Toronto (G.S.H.).

492 References

- 493 Ainslie, N.G., Mackenzie, J.D., and Turnbull, D. (1961) Melting kinetics of quartz and
494 cristobalite. *Journal of Physical Chemistry*, 65, 1718-1724.
- 495 Al-Hasni, B.M., and Mountjoy, G. (2014) A molecular dynamics study of the atomic structure of
496 $x(\text{MgO})_{100-x}(\text{SiO}_2)$, *Journal of Non-Crystalline Solids*, 389, 33- 44.
- 497 Berezhnoi, G.V., and Boiko, G.G. (2005) Defects and Oxygen Diffusion in Metasilicate Melts,
498 *Molecular Dynamics Simulation, Glass Physics and Chemistry*, 31, 145 -154.
- 499 Born, M. (1939) Thermodynamics of Crystals and Melting. *Journal of Chemical Physics*, 40,
500 591-603.
- 501 Bouhifd, M.A., Gruener, G., Mysen, B.O., and Richet, P. (2002) Premelting and calcium
502 mobility in gehlenite ($\text{Ca}_2\text{Al}_2\text{SiO}_7$) and pseudowollastonite (CaSiO_3). *Physics and Chemistry*
503 *of Minerals*, 29, 655-662.
- 504 Bourova, E., Richet, P., and Petit. J.-P. (2006) Coesite (SiO_2) as an extreme case of
505 superheated crystal, An X-ray diffraction study up to 1776 K. *Chemical Geology*, 229, 57-
506 63.
- 507 Brillouin, L. (1938) On Thermal Dependence of Elasticity in Solids. *Physical Review*, 54, 916-
508 917.

- 509 Buchenau, U., and Zorn, R. (2014) A new view of the Lindemann criterion. *Physical Review E*,
510 90, 042312 1-4.
- 511 Ching, W.Y., Murray, R.A., Lam, D.J., and Veal, B.W. (1983) Comparative studies of electronic
512 structures of sodium metasilicate and α and β phases of sodium disilicate. *Physical Review*
513 B, 28, 4724-4735.
- 514 Chuit, C., Corriu, R.J.P., Reye, C., and Young, C.J. (1993) Reactivity of Penta- and
515 Hexacoordinate Silicon Compounds and Their Role as Reaction Intermediates. *Chemical*
516 *Reviews*, 93, 1371-1448.
- 517 Cormack, A.N., Du, J., and Zeitler, T.R. (2002) Alkali ion migration mechanisms in silicate
518 glasses probed by molecular dynamics simulations. *Physical Chemistry and Chemical*
519 *Physics*. 4, 3193-3197.
- 520 Corriu, R.J.P. (1990) Hypervalent species of silicon, structure and reactivity. *Jour.*
521 *Organometallic Chemistry*, 400, 81-106.
- 522 Davis, M.C., Sanders, K.J., Grandinetti, P.J., Gaudio, S.J., and Sabyasachi, S. (2011) Structural
523 investigations of magnesium silicate glasses by ^{29}Si 2D Magic-Angle Flipping NMR.
524 *Journal of Non-Crystalline Solids*, 357, 2787-2795.
- 525 Deer, W.A., Howie, R.A., and Zussman, J. (2013) Introduction to the Rock-Forming Minerals
526 (3rd edition). Mineralogical Society 510p.
- 527 Dimanov, A., and Ingrin, J. (1995) Premelting and high temperature diffusion of Ca in synthetic
528 diopside, an increase of the cation mobility. *Physics and Chemistry of Minerals*, 22, 437-
529 442.
- 530 Eyring, H., Ree, T., and Hirai, N. (1958) Significant structures in the liquid state. I. Proceedings
531 of the National Academy of Sciences, 44, 683-691.

- 532 Farnan, I., and Stebbins, J.F. (1990) High-temperature ^{29}Si NMR investigation of solid and
533 molten silicates. *Journal of the American Chemical Society*, 112, 32-39.
- 534 Fokin, V.M., Zanutto, E.D., Yuritsyn, N.S., and Schmelzer, J.W.P. (2006) Homogeneous crystal
535 nucleation in silicate glasses, A 40 years perspective. *Journal of Non-Crystalline Solids*, 352,
536 2681-2714.
- 537 Frantz, J.D., and Mysen, B.O. (1995) Raman spectra and structure of BaO-SiO_2 , SrO-SiO_2 and
538 CaO-SiO_2 melts at 1600°C. *Chemical Geology*, 121, 155-176.
- 539 Frenkel, J. (1955) *Kinetic Theory of Liquids*. Dover Publications Inc., New York, 488p.
- 540 Fyfe, C.A., Brouwer, D.H., Lewis, A.R., Villaescusa, L.A., and Morris, R.E. (2002) Combined
541 Solid State NMR and X-ray Diffraction Investigation of the Local Structure of the Five-
542 Coordinate Silicon in Fluoride-Containing As-Synthesized STF Zeolite. *Journal of the*
543 *American Chemical Society*, 124, 7770-7778.
- 544 George, A., Richet, P., and Stebbins, J. F. (1998) Cation dynamics and premelting in lithium
545 metasilicate (Li_2SiO_3) and sodium metasilicate (Na_2SiO_3), A high-temperature NMR study.
546 *American Mineralogist*, 83, 1277-1284.
- 547 Gruener, G., Odier, P., De Sousa-Meneses, D., Florian, P., and Richet, P. (2001) Bulk and local
548 dynamics in glass-forming liquids, A viscosity, electrical conductivity, and NMR study of
549 aluminosilicate melts. *Physical Review B*, 64, 024206/1-5.
- 550 Huheey, J.E., Keiter, E.A., and Keiter, R.L. (1993) *Inorganic Chemistry, Principles of Structure*
551 *and Reactivity*, (4th ed.), HarperCollins College Publishers, New York, 964p.
- 552 Kalampounias, A.G., Nasikas, N.K., and Papatheodorou, G.N. (2009) Glass formation and
553 structure in the $\text{MgSiO}_3\text{-Mg}_2\text{SiO}_4$ pseudobinary system: From degraded networks to
554 ioniclike glasses. *Journal of Chemical Physics*, 131, 114513-1–114513-8.

- 555 Koroleva, O.N., Anfilogov, V.N., Shatskiy, A., and Litasov, K.D. (2013) Structure of Na₂O–
556 SiO₂ melt as a function of composition, In situ Raman spectroscopic study. Journal of Non-
557 Crystalline Solids, 375, 62–68.
- 558 Laidler, K.J. (1965) Chemical Kinetics. McGraw-Hill Book Co. New York, 566p.
- 559 Lennard-Jones, J.E., and Devonshire, A.F. (1939) Critical and co-operative phenomena IV. A
560 theory of disorder in solids and liquids and the process of melting. Proceedings of the Royal
561 Society of London A, 170, 464-484.
- 562 Lindemann, F.A. (1910) Über die Berechnung molekulaner Eigenfrequenzen. Zeitschrift für
563 Physik, 11, 609-612.
- 564 Maekawa, H., Maekawa, T., Kawamura, K., Yokokawa, T. (1991) The structural groups of alkali
565 silicate glasses determined from ²⁹Si MAS-NMR. Journal of Non-Crystalline Solids, 127,
566 53-64.
- 567 McDonald, W.S., and Cruickshank, D.W.J. (1967) A Reinvestigation of the Structure of Sodium
568 Metasilicate, Na₂SiO₃. Acta Crystallographica, 22, 37-43.
- 569 McMillan, P.F. (1984) Structural studies of silicate glasses and melts-applications and limitations
570 of Raman spectroscopy. American Mineralogist, 69, 622-644.
- 571 Nasikas, N.K., Chrissanthopoulos, A., Bouropoulos, N., Sen, S., and Papatheodorou, G.N.
572 (2011) Silicate Glasses at the Ionic Limit, Alkaline-Earth Sub-Orthosilicates. Chemistry of
573 Materials 23, 3692–3697.
- 574 Nasikas, N.K., Edwards, T.G., Sen, S., and Papatheodorou, G.N. (2012) Structural
575 Characteristics of Novel Ca–Mg Orthosilicate and Suborthosilicate Glasses, Results from
576 ²⁹Si and ¹⁷O NMR Spectroscopy. Journal of Physical Chemistry B, 116, 2696-2702.
- 577 Nesbitt, H.W., Bancroft, G.M., Henderson, G.S., Ho, R., Dalby, K.N., Huang, Y., and Yan, Z.

- 578 (2011) Bridging, non-bridging and free (O^{2-}) oxygen in Na_2O-SiO_2 glasses, An X-ray
579 Photoelectron Spectroscopic (XPS) and Nuclear Magnetic Resonance (NMR) study. Journal
580 of Non-Crystalline Solids, 357, 170–180.
- 581 Nesbitt, H.W., Bancroft, G.M., Henderson, G.S., Sawyer, R., Secco, R.A., (2015a). Direct and
582 Indirect Evidence for Free Oxygen (O^{2-}) in MO-Silicate Glasses and Melts (M = Mg, Ca,
583 Pb). Am. Mineral. 100, 2566-2578.
- 584 Nesbitt, H.W., Henderson, G.S., Bancroft, G.M., and Ho, R. (2015b) Experimental evidence for
585 Na coordination to bridging oxygen in Na-silicate glasses, Implications for spectroscopic
586 studies and for the modified random network model. Journal of Non-Crystalline Solids, 409,
587 139-148.
- 588 Nesbitt, H.W., Bancroft, G.M., Thibault, Y., Sawyer, R., and Secco, R.A. (2015c) Reply to the
589 comment by Malfait on “Spectroscopic studies of oxygen speciation in potassium silicate
590 glasses and melts”. Canadian Journal of Chemistry, 93, 581–587.
- 591 Retsinas, A., Kalamounias, A.G., and Papatheodorou, G.N. (2014) Reaching the ionic limit in
592 the $(1-X)[Ca_{0.5}-Mg_{0.5}]O-XSiO_2$ pseudo binary glass system with $0.5 < X < 0.27$: Glass
593 formation and structure. Journal of Non-Crystalline Solids, 383, 38-43.
- 594 Richet, P., and Fiquet G. (1991) High-temperature heat capacity and premelting of minerals in
595 the system $MgO-CaO-Al_2O_3-SiO_2$. Journal of Geophysical Research, 96, 445-456.
- 596 Richet, P., Ingrin, J., Mysen, B.O., Courtial, P., and Gillet, P. (1994) Premelting effects in
597 minerals, an experimental study. Earth and Planetary Science Letters, 121, 589-600.
- 598 Richet, P., Leclerc, F., and Benoist, L., (1993) Melting of forsterite and spinel with implication
599 for the glass transition of the Mg_2SiO_4 liquid. Geophysical Research Letters, 20, 1675-1678.
- 600 Richet, P., and Mysen, B.O. (1999) High-temperature dynamics from Raman spectroscopy in

- 601 cristobalite (SiO₂) and carnegieite (NaAlSiO₄). Geophysical Research Letters, 26, 2286-
602 2286.
- 603 Richet, P., Mysen, B.O., and Andrault, D. (1996) Melting and premelting of silicates, Raman
604 spectroscopy and X-ray diffraction of Li₂SiO₃ and Na₂SiO₃. Physics and Chemistry of
605 Minerals, 23, 157-172.
- 606 Richet, P., Mysen, B.O., and Ingrin, J. (1998) High-temperature X-ray diffraction and Raman
607 spectroscopy of diopside and pseudowollastonite. Physics and Chemistry of Minerals, 25,
608 401-414.
- 609 Richet, P., and Neuville, D.R. (1992) Thermodynamics of Silicate Melts. Configurational
610 Properties (Chap. 5). *in* Thermodynamic Data, Systematics and Estimation. (e.d S.K.
611 Saxena). Springer-Verlag, New York. p. 132-161.
- 612 Richet, P., and Ottonello, G. (2014) The Earth as a multiscale quantum-mechanical system.
613 Comptes Rendus Geoscience, 346, 317-325.
- 614 Sawyer, R., Nesbitt, H.W., Bancroft, G.M., Thibault, Y., and Secco, R.A. (2015) Spectroscopic
615 studies of oxygen speciation in potassium silicate glasses and melts. Canadian Journal of
616 Chemistry, 93, 60–73.
- 617 Sawyer, R., Nesbitt, H.W., and Secco, R.A. (2012) Three types of oxygen in K₂O-SiO₂ glasses,
618 an X-ray photoelectron spectroscopy (XPS) study. Journal of Non-Crystalline Solids, 358,
619 290-302.
- 620 Schairer, J. F., and Bowen, N. L. (1955) The system K₂O-Al₂O₃-SiO₂. American Journal of
621 Science, 253,681-746.
- 622 Sen, S., and Tangeman, J. (2008) Evidence for anomalously large degree of polymerization in
623 Mg₂SiO₄ glass and melt. American Mineralogist, 93, 946-949.

- 624 Sen, S., Maekawa, H., and Papatheodorou, G.N. (2009) Short-range structure of invert glasses
625 along the pseudo-binary join $\text{MgSiO}_3\text{-Mg}_2\text{SiO}_4$: results from ^{29}Si and ^{25}Mg NMR
626 spectroscopy. *Journal of Physical Chemistry*, 113, 15243-15248.
- 627 Seryotkin, Y.V., Sokol, E.V., and Kokh, S.N. (2012) Natural pseudowollastonite: Crystal
628 structure, associated minerals, and geological context. *Lithos*, 134-135, 75-90.
- 629 Speight, J.G. (2005) *Lange's Handbook of Chemistry 70th Anniversary Edition*. McGraw Hill
630 Standard Handbook, New York, Table 4.11, p. 4.41-4.51.
- 631 Stebbins, J.F. (1991) NMR evidence for five-coordinated silicon in a silicate glass at atmospheric
632 pressure. *Nature*, 351m 638-639.
- 633 Téqui, C., Grinspan, P., and Richet, P. (1992) Thermodynamic properties of alkali silicates, Heat
634 capacity of Li_2SiO_3 and lithium silicate melts. *Journal of the American Ceramics Society*,
635 75, 2601-2604.
- 636 Thiéblot, L., Téqui, C., and Richet, P. (1999) High-temperature heat capacity of grossular
637 ($\text{Ca}_3\text{Al}_2\text{Si}_3\text{O}_{12}$), enstatite (MgSiO_3), and titanite (CaTiSiO_5). *Amer. Mineral.* 84, 848-855.
- 638 Wagstaff, F.E. (1969) Crystallization and Melting Kinetics of Cristobalite. *Journal of the*
639 *American Ceramic Society*, 52, 650-654.
- 640 Wolf, G.H., Durben, D.J., and McMillan, P.F. (1990) High-pressure Raman spectroscopic study
641 of sodium tetrasilicate ($\text{Na}_2\text{Si}_4\text{O}_9$) glass. *Journal of Chemical Physics*, 93, 2280-2288.
- 642 Wolf, G.H., and Jeanloz, R. (1984) Lindemann Melting Law, Anharmonic Correction and Test
643 of Its Validity for Minerals. *Journal of Geophysical Research B*, 89, 7821-7835.
- 644 Yang, H., and Prewitt, C.T. (1999) On the crystal structure of pseudowollastonite (CaSiO_3).
645 *American Mineralogist*, 84, 929-932.

646 **Figure Captions**

647 Fig. 1. Changes to unit cell parameters for Na_2SiO_3 and heat capacities of numerous crystals as a
648 function of temperature (T). (a) Changes to the 'a', 'b' and 'c' unit cell parameters of
649 Na_2SiO_3 as a function of T, cast as a ratios, a/a_0 , b/b_0 and c/c_0 . The denominator
650 represents the value of the cell parameter at the lowest temperature measured. For clarity,
651 the a/a_0 ratios are displaced to a lower value by 0.005 units. (b) Mean heat capacity (C_m)
652 of crystals versus T where $C_m = (H_T - H_{273}) / (T - 273)$ with H being heat content (Richet and
653 Fiquet, 1991). The premelting region extends from the inflection in C_m to the melting
654 point (e.g., ~1200 to 1362 K for Na_2SiO_3). Dashed curves are extrapolations of fits to the
655 C_m data, excluding measurements in the premelting range. The diopside data are
656 displaced upward by one unit. Fig. 2. Schematic of the structural consequences of
657 Reaction (1a) where two, initially separate SiO_3 chains shown in (a), undergo reaction to
658 produce a cross-chain linkage through production of a Q^3 species, as shown in (b). A
659 schematic of the activated complex is illustrated in (c).

660 Fig. 3. ^{29}Si MAS NMR and Raman spectra of Na_2SiO_3 for glass and crystal. Experimental data
661 are represented by dots in each diagram. Solid curves represent the introduced Q^1 , Q^2 and
662 Q^3 species peaks. The sum of the Q species contributions are also represented by solid
663 curves. (a) NMR spectrum of the glass collected at ambient temperature. The data, fit and
664 Q species abundances are taken from Nesbitt et al. (2011). (b) Raman spectrum of the
665 glass collected at 298 K. The experimental data are represented by dots and are taken
666 from Frantz and Mysen (1995, their Fig. 9). Peak assignments and the partial fit are
667 discussed in the text. The fit is not intended to be complete but was performed solely to
668 establish the approximate locations of the major Q species peaks for comparison with
669 those of the crystal. (c) Raman spectrum of the crystal collected just below the melting

670 temperature (data from Richet et al., 1996). The fit is entirely unconstrained. Peak
671 assignments and fit are discussed in the text.

672 Fig. 4. Schematic diagram of the melting of $\text{Na}_2\text{SiO}_3(\text{c})$. (a) Illustrates the attack of O^{2-} on a Si
673 center to form a transition state complex (dotted oval) according to Reaction (3b). (b)
674 Schematic diagram showing the products of Reaction (3b), which are two Q^1 species
675 terminating two SiO_3 chains and destroying the chain structure to produce melt. (c) a
676 pseudo 3-dimensional rendering of the activated complex.

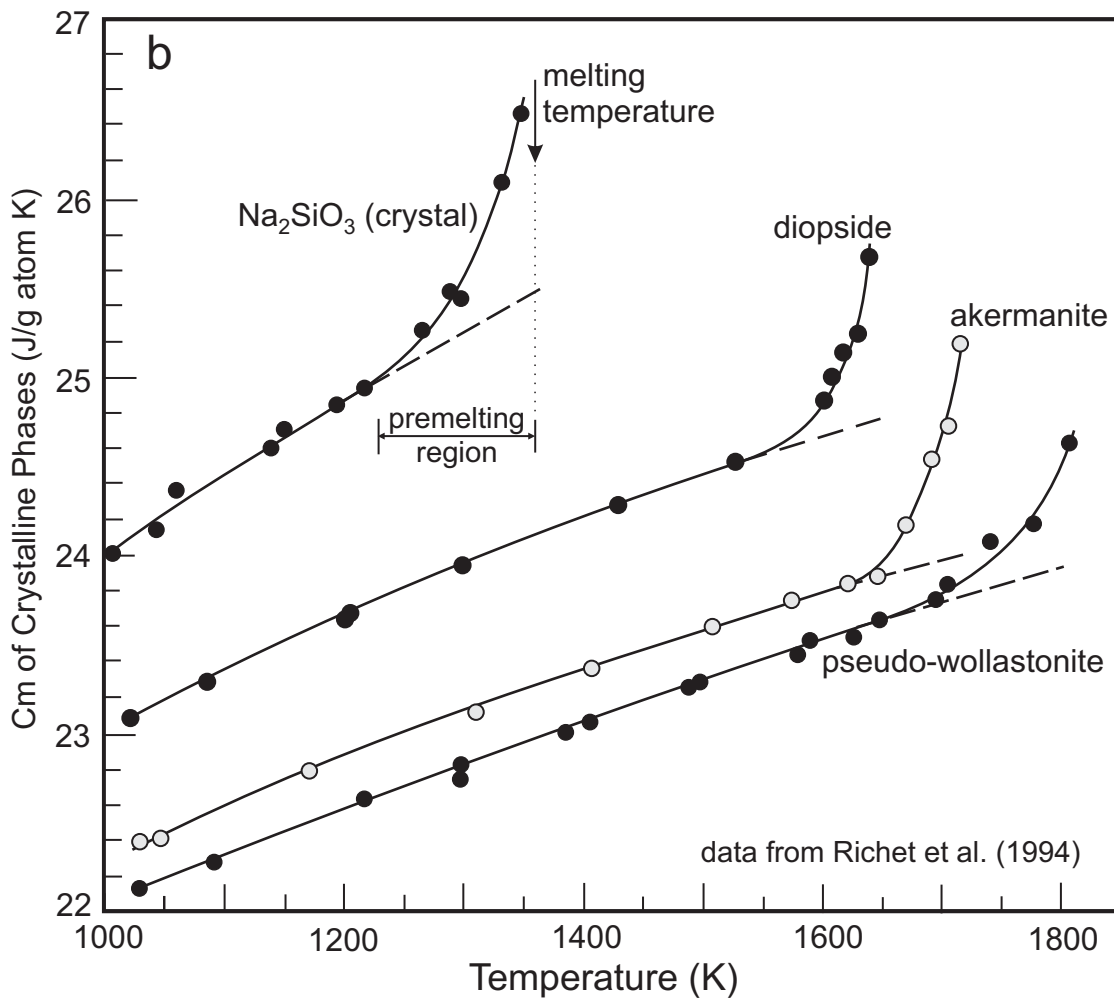
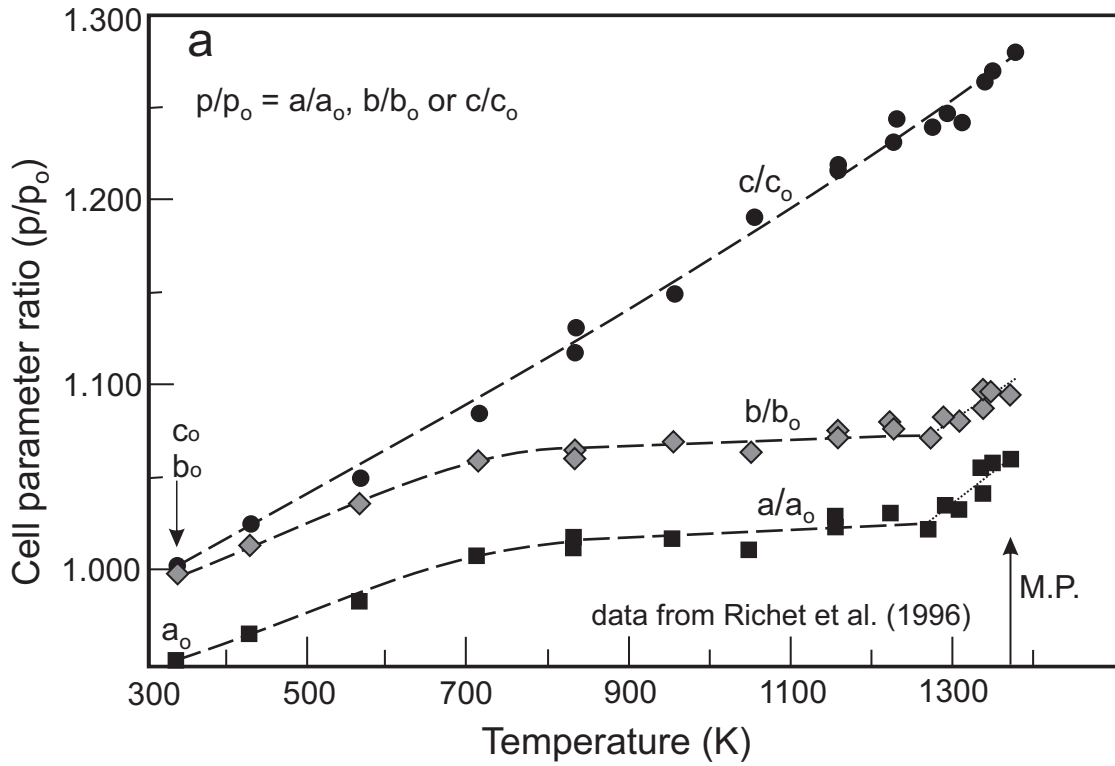


Fig. 1

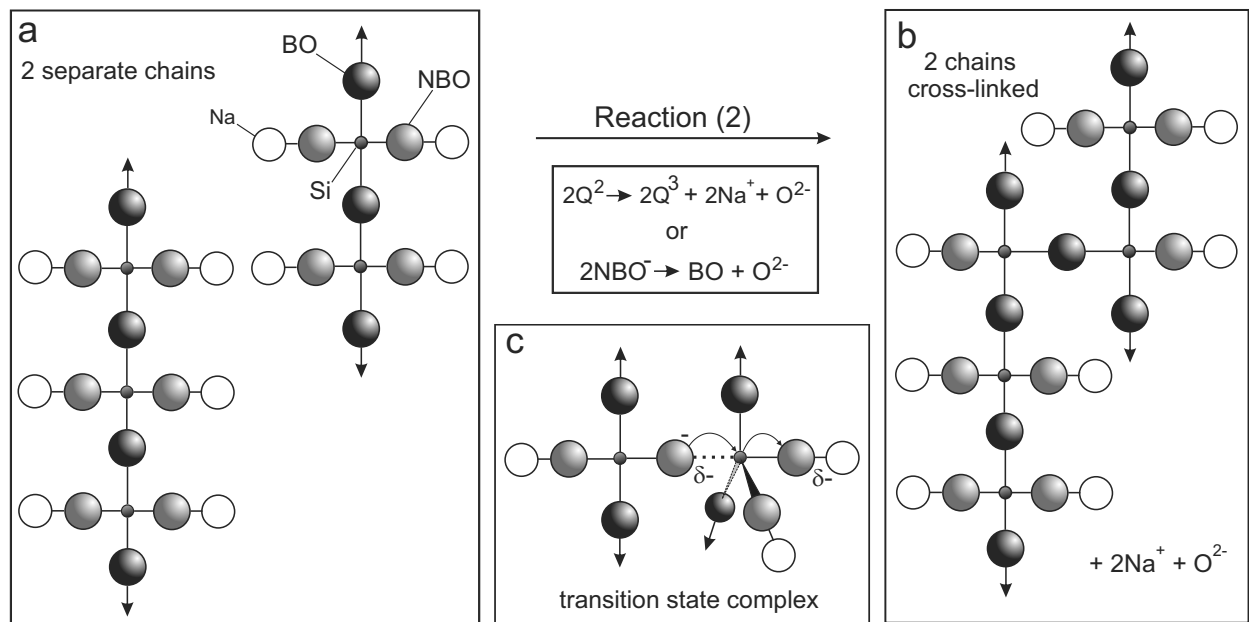


Fig. 2

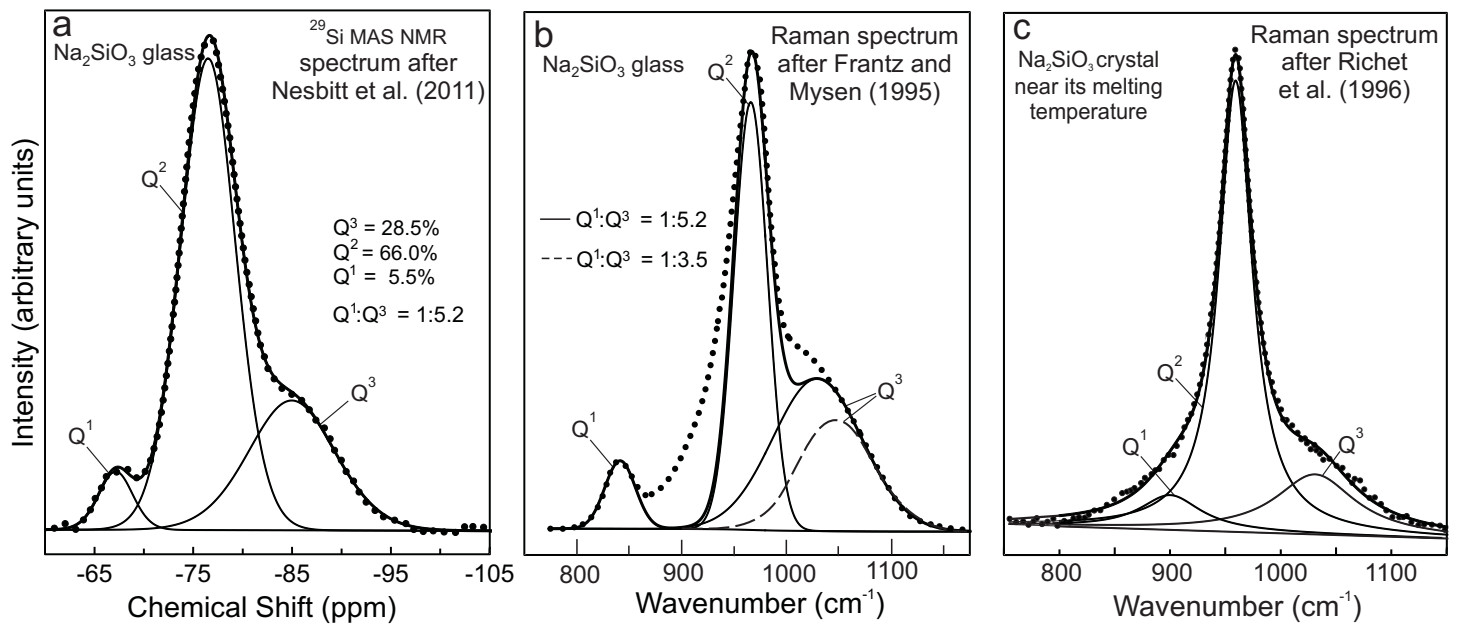


Fig. 3

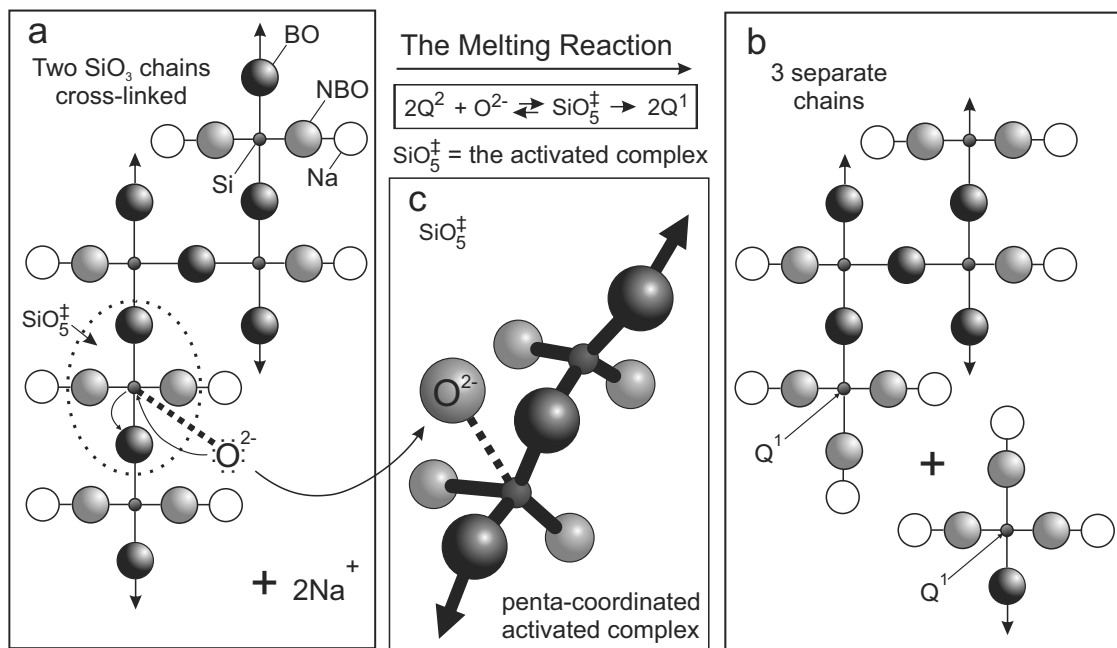


Fig. 4